







Article

Optical Characterization of Cesium Lead Bromide Perovskites

Fabio De Matteis ^{1,*}, Francesco Vitale ¹, Simone Privitera ¹, Erica Ciotta ¹, Roberto Pizzoferrato ¹, Amanda Generosi ², Barbara Paci ², Lorenzo Di Mario ², Jacopo Stefano Pelli Cresi ², Faustino Martelli ³ and Paolo Proposito ¹

¹ Department of Industrial Engineering, University of Rome Tor Vergata, Via del Politecnico 1, 00133 Rome, Italy; francesco.vitale.mim@gmail.com (F.V.); privi.simone@hotmail.it (S.P.); Erica.Ciotta@uniroma2.it (E.C.); pizzoferrato@uniroma2.it (R.P.); proposito@roma2.infn.it (P.P.)

² Istituto di Struttura della Materia (ISM), Consiglio Nazionale delle Ricerche CNR, Via del Fosso del Cavaliere 100, 00133 Rome, Italy; amanda.generosi@ism.cnr.it (A.G.); Barbara.Paci@ism.cnr.it (B.P.); lorenzo.dimario@ism.cnr.it (L.D.M.); pcsj22@gmail.com (J.S.P.C.)

³ Istituto per la Microelettronica e i Microsistemi (IMM), Consiglio Nazionale delle Ricerche CNR, Via del Fosso del Cavaliere 100, 00133 Rome, Italy; faustino.martelli@cnr.it

* Correspondence: fabio.dematteis@uniroma2.it; Tel.: +39-6-72594521

Received: 3 April 2019; Accepted: 25 May 2019; Published: 28 May 2019



Abstract: CsPbBr₃ and Cs₄PbBr₆ perovskite powders have been synthesized through a relatively simple low-temperature and low-cost method. Nanocrystalline films have also been deposited from solutions with four different molar compositions of binary salt precursors. Optical absorption, emission and excitation spectra have been performed in the UV-visible spectral range while X-ray diffraction (XRD) has been recorded to characterize the nanocrystal morphology for the different molar compositions. A preferential orientation of crystallites along the (024) crystalline plane has been observed as a function of the different deposition conditions in films growth. All the crystals show an absorption edge around 530 nm; Tauc plots of the absorption returned bandgaps ranging from 2.29 to 2.35 eV characteristic of CsPbBr₃ phase. We attribute the UV absorption band peaked at 324 nm to the fundamental band-to-band transition for Cs₄PbBr₆. It was observed that the samples with the most ordered Cs₄PbBr₆ crystals exhibited the most intense emission of light, with a bright green emission at 520 nm, which are however due to the luminescence of the inclusion of CsPbBr₃ nanoclusters into the Cs₄PbBr₆. The latter shows instead an intense UV emission. Differently, the pure CsPbBr₃ powder did not show any intense fluorescent emission. The excitation spectra of the green fluorescent emission in all samples closely resemble the CsPbBr₃ absorption with the peculiar dip around 324 nm as expected from density of state calculations reported in the literature.

Keywords: cesium lead bromide perovskites; fluorescence; Cs₄PbBr₆; nanocrystals

1. Introduction

Calcium titanium oxide mineral (CaTiO₃) was the first crystal to be named perovskite. Then its name has been extended to a class of compounds which have the same type of crystal structure, known as the perovskite structure. Many different cations can be embedded in this structure, allowing the development of diverse engineered materials.

Metal halide perovskites, with the chemical formula $A_nBX_{(2+n)}$, where A and B are respectively the monovalent and divalent (Pb, Sn) cations and X is a monovalent anion (Cl, Br, I), are a large family of materials with a wide range of compositional and structural flexibilities [1].

Perovskites are typically divided into two main categories depending on the chemical component of the cation A. When A is an organic cation (e.g., the well-known methyl ammonium MA = CH₃NH₃⁺)

and B an inorganic one, the perovskite is considered as hybrid organic–inorganic. On the contrary, if A is inorganic (mostly Cs^+) the perovskite is all-inorganic.

Hybrid organic–inorganic metal halides (HOIMHs) have been extensively investigated for a wide range of applications, such as photovoltaics [2–7], light emitting diodes (LED) or lasers [8–13], radiation detection [14], and down-converting phosphors [15–17]. Interesting carrier transport properties have been observed in Pb- and Sn-based 3D halide perovskites [18,19]. HOIMHs, like MAPbI_3 , have been broadly studied as solar absorber materials in photovoltaic cells [20].

Distinct crystalline forms with the general formula $A_n\text{BX}_{2+n}$ give rise to an extended perovskite family [21]. They differ in the spatial coordination of the metal-halide octahedra XBr_6^{4-} where the value of n determines the perovskite's structural dimensionality expressing the coordination of octahedra: $n = 1$ characterizes three-dimensional (3D) perovskites with corner-shared octahedra along every axis, $n = 4$ identifies zero-dimensional (0D) perovskites with isolated octahedra, as shown in Figure 1a for cesium lead perovskites. Efficient photoluminescence is associated to the intrinsic geometric structures or the different network dimensionalities due to the occurrence of quantum confinement into the isolated octahedra of 0D-crystals [22]. The Frenkel excitons result self-trapped in correspondence of the octahedron centered on the Pb ions: the lower the perovskite structural dimensionality the higher the binding energy of the electron-hole couple. The 3D CsPbBr_3 and the 0D Cs_4PbBr_6 structures show an exciton binding-energy of 19–62 meV and 353 meV, respectively [22]. The latter value leads to a dominant radiative recombination in correspondence of the lead ion sites, as shown by calculations based on density functional theory (DFT) [23,24]. The photoluminescence quantum yield (PLQY) is reported to differ considerably between the two structures from 0.1% (3D) to 45% (0D) [22,25]. The high PLQY of the 0D phase suggests the application of the inorganic perovskite to solid state optoelectronic devices such as LEDs or solar cells making critical a proper understanding of this perovskite. The origin of the green photoluminescence, however, has been subject of a large debate: Nikl et al. [26] were the first to suggest that unavoidable CsPbBr_3 nanocrystal impurities in Cs_4PbBr_6 gives origins to the green photoluminescence. A recent article has yielded further convincing experimental evidence of the latter [27].

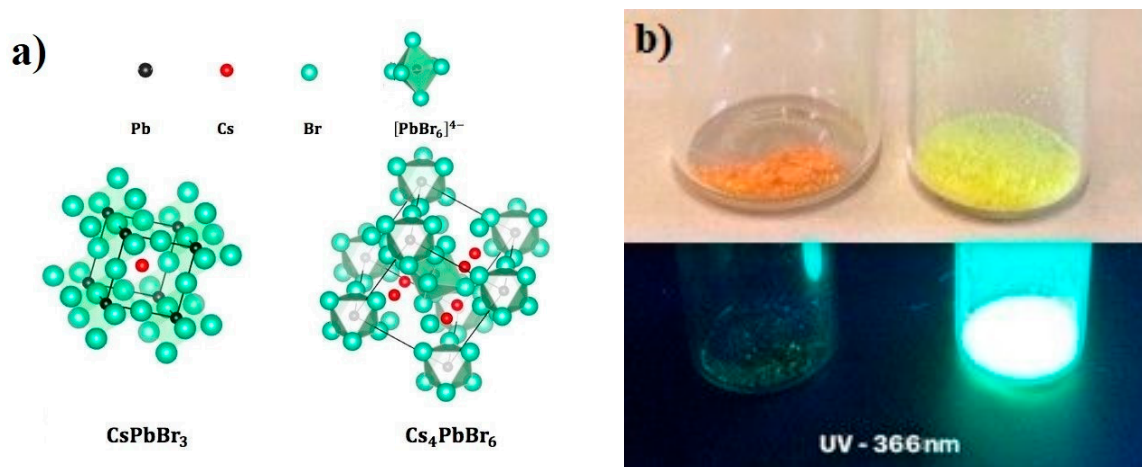


Figure 1. (a) Crystal structures of CsPbBr_3 , and Cs_4PbBr_6 perovskite; (b) photos of powders of Cs_4PbBr_6 orange crystals and DMSO washed Cs_4PbBr_6 yellow crystals with room light (top) and UV-A light (bottom).

With our contribution, we aim to bring further evidence that the efficient green fluorescence comes from the CsPbBr_3 nano-inclusions inside the Cs_4PbBr_6 matrix. The Cs_4PbBr_6 perovskite phase is not fluorescent in the visible range, but it shows a strong UV luminescence.

2. Materials and Methods

2.1. Synthesis of CsPbBr₃ and Cs₄PbBr₆ Powders

An equimolar mixture of CsBr (0.25 M; 212 mg) and PbBr₂ (0.25 M; 370 mg) was dissolved in 1 mL dimethyl sulfoxide (DMSO) at room temperature. DMSO is a good aprotic polar solvent commonly used to dissolve inorganic salts and small molecules. The mixture was stirred for 1 hour and heated at 120 °C for 3 hours with the result of the precipitation of Cs₄PbBr₆ grains together with undesired CsPbBr₃ and CsPb₂Br₅ phases. In the absence of any washing, an orange powder was obtained largely composed of CsPbBr₃. The precipitate was washed with DMSO, a procedure that was meant for removing the undesired phases and, due to the poor solubility of Cs₄PbBr₆, the washed powder (enriched with Cs₄PbBr₆) appeared with a brilliant green-yellow color and exhibited a bright and strong photoluminescence under UV light, in contrast with the starting (predominantly CsPbBr₃) powder which appeared weakly or not fluorescent (Figure 1b). In both cases, the powders had been dried at 70 °C overnight in an evacuated oven.

The ternary diagram (Cs-Pb-Br) predicted the presence of both Cs₄PbBr₆ and CsPbBr₃ crystalline phases for an equimolar ratio between the two precursors. However, the content of a certain phase can be determined, to some extent, by the synthesis procedure. Indeed, if the CsBr concentration is increased in the precursor solution, the formation of Cs₄PbBr₆ becomes dominant [9]. This phase is thermodynamically favored since the enthalpy of formation for the 0D phase (Cs₄PbBr₆) is lower than the 3D one (CsPbBr₃) [28].

To this purpose we prepared precursor solutions in DMSO of mixed CsBr and PbBr₂ salts with different molar ratios and deposited films on glass slides from such solutions.

2.2. Synthesis of Cs₄PbBr₆ Nanocrystal (NC) Films

CsBr and PbBr₂ were dissolved at different relative molar ratios of 1:1, 2:1, 3:1 and 4:1 in order to control the final product composition. Since the CsBr is scarcely soluble in DMSO at high concentration, the two salts were initially dissolved in different solvents: aprotic DMSO for PbBr₂ (0.1 M: 370 mg in 10 mL) and deionized water for CsBr (1M: respectively 212 mg, 424 mg, 636 mg and 848 mg in 1 mL). Then the CsBr/H₂O solution was slowly poured into the PbBr₂/DMSO solution and the mixture was stirred for 3 hours at RT. The solution was centrifuged at 5000 rpm for 10 min and a yellowish precipitate was separated from the supernatant. The precipitate in DMSO was spin-coated on 2 × 2 cm² glass substrates to obtain nanocrystal (NC) films. The spin-coating procedure was performed in a glove box with inert nitrogen atmosphere and a spin velocity of 1000 rpm for 30 s. During the spinning, 100 μL of acetone were sprayed on the sample to favor a rapid nucleation of the crystallites due to its anti-solvent property with respect to the inorganic perovskites [9]. The films were finally annealed on a hot-plate to complete the solvent evaporation and to obtain the films at different molar ratios shown in Figure 2.

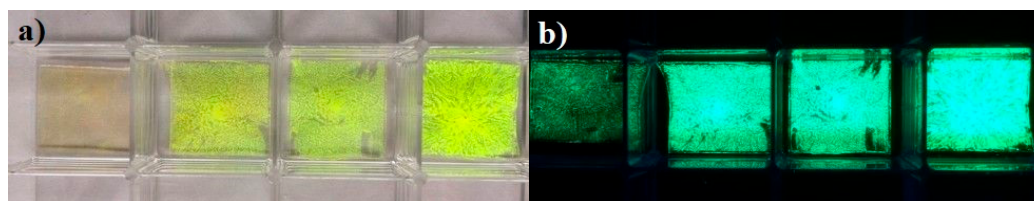


Figure 2. (a) Films of perovskite nanocrystals (NCs) with precursor molar ratios, respectively, from the left 1:1, 2:1, 3:1 and 4:1 under room light; (b) the same under UV-A illumination (broad band 366 nm).

2.3. X-Ray Diffraction Measurements

X-ray diffraction measurements (XRD) were performed in reflection mode on a Panalytical Empyrean Diffractometer, using the $k\alpha$ fluorescence line of a Cu-anode emitting tube as X-ray source

(40kV–40mA). Bragg Brentano configuration was used as incident optical pathway ($1/4^{\circ}$ – $1/2^{\circ}$ divergent slits) and a solid-state hybrid Pix'cel 3D detector, working in 1D linear mode, accomplished the detection. Samples were studied in the range $10^{\circ} < 2\theta < 50^{\circ}$.

2.4. Spectral Measurements

Absorption spectra were collected in the spectral interval 300–600 nm by means of a double beam Shimadzu UV-2500 equipped with a Xenon lamp and an integrating sphere for diffuse reflection measurements. The steady-state luminescence spectra were excited by the 458 nm line of an Ar⁺ laser with 0.014 W/mm² and collected by a compact spectrophotometer (Flame, OceanOptics, Largo, FL, USA) [29]. A different set-up has been used for the time-resolved luminescence and to study the UV emission from the samples. For those measurements, different lines (in the 260–320 nm range) of an Optical Parametric Amplifier (OPA) have been used. The pulse length was about 50 fs and the repetition frequency 1 kHz. The luminescence was revealed with the spectrometer Halcyon of the Ultrafast Systems. The time resolved measurements were made with the time correlated single photon counting (TCSPC) method with an instrument response function (IRF) of 0.9 ns. The fluences were in the 0.1–100 $\mu\text{J}/\text{cm}^2$ range. The excitation spectra were recorded using a conventional 90° geometry on a dedicated laboratory setup equipped with a 200 W continuous Hg(Xe) discharge lamp (Oriel instruments, Stratford, CT, USA), an excitation 25-cm monochromator (Photon Technology International, Inc., Birmingham NJ, USA) and an emission 25-cm monochromator (Cornerstone 260, Stratford, CT, USA) equipped with specific excitation-rejection filters and a R3896 photomultiplier (Hamamatsu Photonics Corp., Bridgewater, NJ, USA) [30,31].

3. Results and Discussion

Microcrystal powders have been characterized by X-ray diffraction measurements in order to investigate the distribution of the different crystalline phases. Figure 3a shows the spectra of the samples obtained with the first synthesis (equimolar mixture) without any washing procedure (orange powder, Figure 1b). Figure 3b shows the spectra after washing with DMSO (yellow powder, Figure 1b).

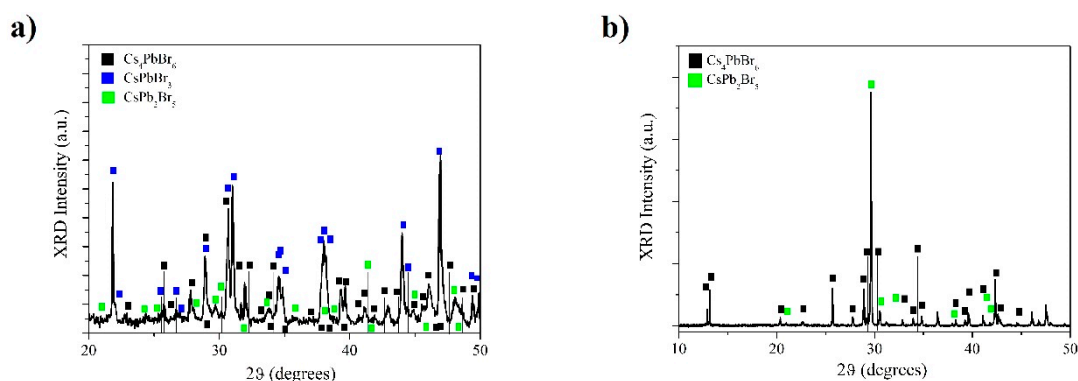


Figure 3. XRD spectra of perovskite: (a) unwashed powder; (b) powder washed with DMSO.

The XRD patterns, cross-checked with powder diffraction databases, perfectly match the coexistence of three phases. The 3D CsPbBr₃ phase is monoclinic with lattice constants $a = 5.83 \text{ \AA}$, $b = 5.83 \text{ \AA}$, and $c = 5.89 \text{ \AA}$ (ICDD Nr 00-018-0364, [32] peaks are marked by a blue square). The 0D Cs₄PbBr₆ phase is rhombohedral with lattice constants $a = 13.73 \text{ \AA}$, $b = 13.73 \text{ \AA}$, and $c = 17.32 \text{ \AA}$ (ICDD Nr 01-073-2478, [33] the reflections are labelled by a black square). A third 3D spurious phase CsPb₂Br₅ was also detected, corresponding to a tetragonal crystal system: $a = 8.48 \text{ \AA}$, $b = 8.48 \text{ \AA}$, and $c = 15.25 \text{ \AA}$ (ICDD Nr 01-025-0211, [34] the peaks are highlighted by a green square).

According to the literature [8,35], the characteristic crystalline phase signatures attributed to 3D-CsPbBr₃ and 0D-Cs₄PbBr₆ respectively, are present in the two samples: the first sample has a

dominant contribution from the monoclinic 3D phase while the second one from the rhombohedral 0D phase with traces from the tetragonal one.

Subsequently, measurements were performed in the same experimental conditions on the films obtained from solutions at different molar ratios of CsBr:PbBr₂ (4:1, 3:1, 2:1 and 1:1) to determine the effect of deposition on the crystallographic properties of the material and the effects of precursor molar ratio as shown in Figure 4.

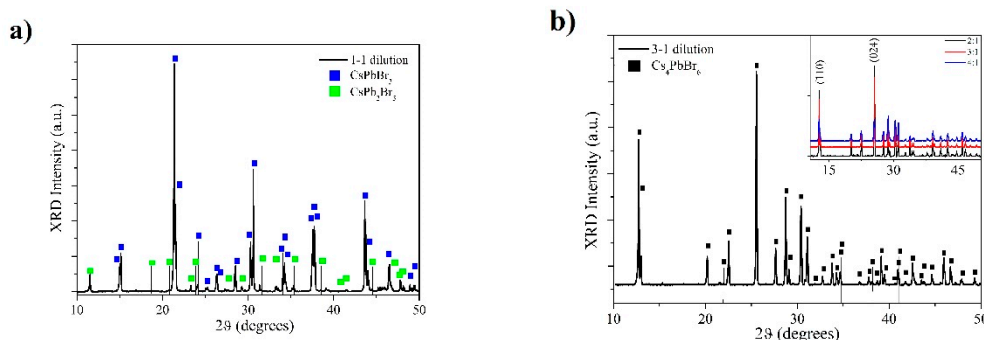


Figure 4. XRD spectra of perovskite films obtained from (a) 1:1 and (b) 3:1 precursor solution. In the inset of figure (b), patterns collected from films at different molar ratios are shown.

Peaks at $2\theta = 21.40^\circ$, $2\theta = 30.60^\circ$ and $2\theta = 43.60^\circ$ are clearly present in the 1:1 film, confirming the presence of the 3D CsPbBr₃ perovskite dominant phase (see Figure 4a). Moreover, peaks at $2\theta = 12.80^\circ$, $2\theta = 30.20^\circ$ and $\vartheta = 38.90^\circ$ characterize the XRD spectra of the 3:1 film, leading to the attribution of the 0D-Cs₄PbBr₆ perovskite phase (see Figure 4b). Similar XRD spectra are obtained for films with exceeding CsBr precursor with respect to the PbBr₂, i.e., 2:1 and 4:1 (see inset in Figure 4b).

All films presented polycrystalline texture, therefore all possible diffraction peaks relative to the structure were observed. In a perfectly powder-like material, i.e., completely anisotropic, the relative intensities of the different reflections are theoretically stated (for example the intensity of the diffraction peak relative to the (110) crystalline plane is expected to be 93% while that of the (024) one is 50%), while preferential orientation of crystallites can create a systematic variation in the diffraction peak intensities.

This specific effect was observed in the films as a function of the varied deposition conditions and was quantitatively analyzed studying the variation of the (024)/(110) reflections intensity ratio as a function of molar concentration ratio as shown in Figure 5. As visible, the thermodynamically favored (110) peak decreases at higher molar ratio values down to a minimum reached at a (3:1) ratio: a trend could be observed and correlated to a similar behavior of the fluorescence intensity, as will be discussed below.

Furthermore, the films grain size analysis was also performed, by means of the Scherrer formula:

$$D = \frac{K\lambda}{\beta C \cos \theta'} \quad (1)$$

with K being the Scherrer constant (0.89), λ the X-ray wavelength (0.15418 nm K $_{\alpha}$ Cu anode), β the average full width half maximum of the crystalline reflections and ϑ the scattering angle. Grain size was calculated for the differently composed films and the average size was found to be comparable in all samples: $D = (80 \pm 5)$ nm. The value of the grain size thus obtained is comparable to published results for this type of preparation of perovskite NCs [36].

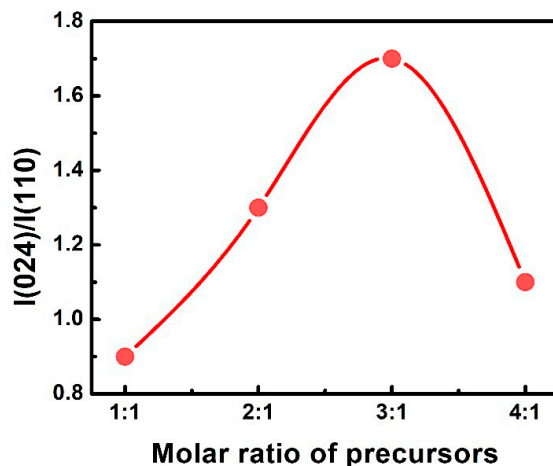


Figure 5. Intensity ratio of the (024) reflection vs. the (110) reflection as a function of different film concentrations. A trend of the structural rearrangement can be observed occurring as a function of the relative concentration parameter.

The absorption spectra of the films prepared with different molar ratios are reported in Figure 6. Extended absorption in the UV spectral range (down to 280 nm) highlights interesting features of the optical behavior of this material. Two main absorption structures are recognized in the spectra of all the films: one in the UV and the other in the visible spectral range [9,24,37]. The structure which peaked at 324 nm corresponds to the band–band excitation for Cs_4PbBr_6 crystal as reported by direct measurements and density of state calculations [38]. The absorption in the visible region is characteristic of the CsPbBr_3 with an absorption edge at wavelength below 550 nm. The inset in Figure 6 shows the Tauc plots for the absorption spectra which allow the determination of the absorption edges for the different samples. The data are reported in Table 1. The 1:1 film has an absorption edge at 2.29 eV ($\lambda = 541$ nm) while the others (3:1 and 4:1) at 2.35 eV ($\lambda = 528$ nm), in very good agreement with the values reported in the literature [25]. The 2:1 sample shows an absorption edge intermediate between the two.

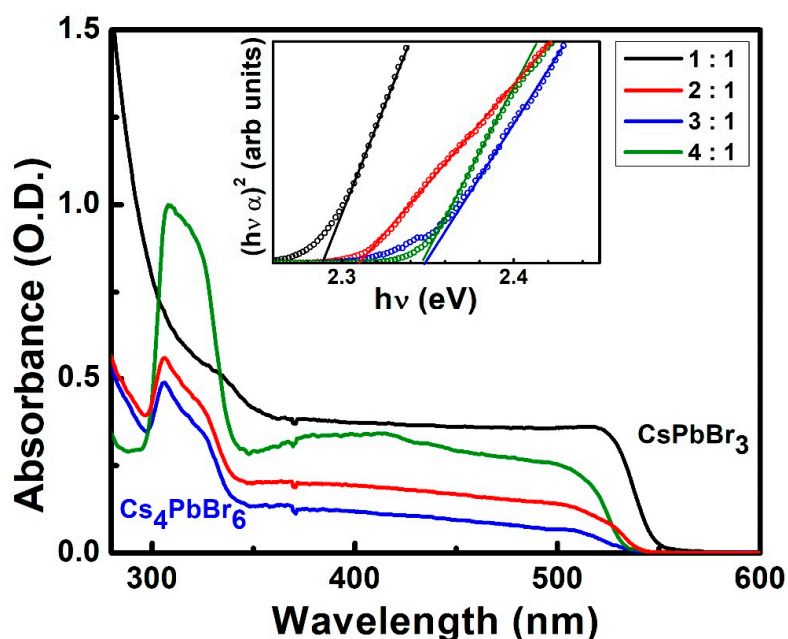


Figure 6. Absorption spectra of the films with different molar ratios of precursors indicated in the label. The inset reports the Tauc plots for the determination of the absorption edge.

Table 1. Edges of absorption for each samples.

Sample	Edge of Absorption	
	(nm)	(eV)
1:1	541	2.29
2:1	537	2.31
3:1	528	2.35
4:1	528	2.35

The onset of the absorption at 2.35 eV is apparently in contrast with the 3.3 eV band gap [39] expected for the presence of Cs_4PbBr_6 phase (3:1 and 4:1 samples). However, it has been showed that CsPbBr_3 inclusion in Cs_4PbBr_6 crystals, even at a very low weight ratio, can generate components in the visible absorption spectra in addition to the UV absorption band characteristic of the Cs_4PbBr_6 phase [40]. Therefore, the absorptions of both phases are present in the spectra of all samples with different contributions: the Cs_4PbBr_6 increases from 1:1 to 4:1 samples while the other decreases. The absorption edge of the CsPbBr_3 phase moves from the bulk value 2.29 eV in the equimolar sample to 2.35 eV as a consequence of quantum confinement effects for the electronic excitation of CsPbBr_3 nano-inclusions [37,41,42]. Tian and Scheblykin [43] have recently sounded a note of caution about the absorption measurements in this type of samples due to poor surface coverage, high optical density of individual crystals, and light scattering. Therefore, one should be cautious to draw too detailed and quantitative conclusions from the absorption measurements.

The photoluminescence spectra are shown in Figure 7. An intense green photoluminescence (PL) emission band is present with a peak at 520 nm for the excitation wavelength of 458 nm and a radiant flux of 14 mW/mm². An increase of the emitted intensity was observed with the increase of the molar ratio of Cs/Pb precursors in accordance with the literature [36,43,44]. The trend observed for the fluorescence intensity with the increase of the CsBr content in the precursor solution is shown in the inset in Figure 7 and follows the increase of concentration of CsPbBr_3 inclusions in the different samples. The 4:1 precursor molar ratio, which represents the right stoichiometry in order to obtain the Cs_4PbBr_6 phase, maximizes the formation of this phase at expenses of the other type and hence of the possibility of inclusions. That could explain the decrease of the intensity for 4:1 sample in agreement with the attribution of the green fluorescence to CsPbBr_3 inclusions in the Cs_4PbBr_6 .

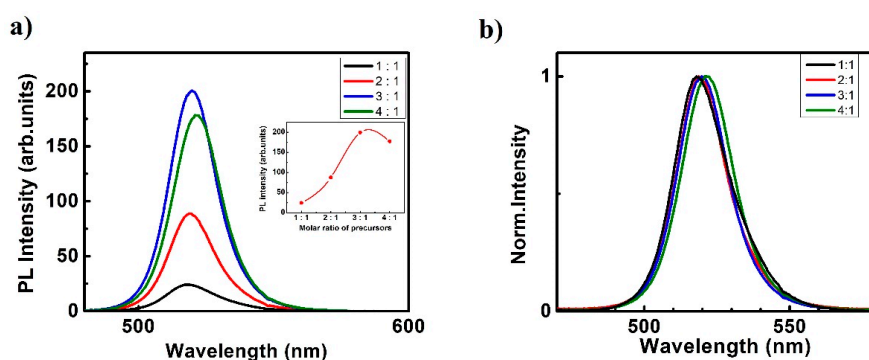


Figure 7. (a) Photoluminescence (PL) spectrum for different molar ratio of precursors. Excitation wavelength was 458 nm. The inset shows the peak intensity as a function of precursor composition. (b) Normalized PL spectra.

Time correlated single photon counting (TCSPC) measurements have been performed in order to study the radiative decay originating the VIS-PL in the different samples. The radiative decay of the PL at 521 nm for excitation at 360 nm is shown in Figure 8; the results of a fit to a double exponential decay model have been reported in Table 2. The values do not significantly change within the excitation

intensity range used. Similarly, no significant difference is observed for the different samples indicating that for all the samples the green luminescence has the same origin.

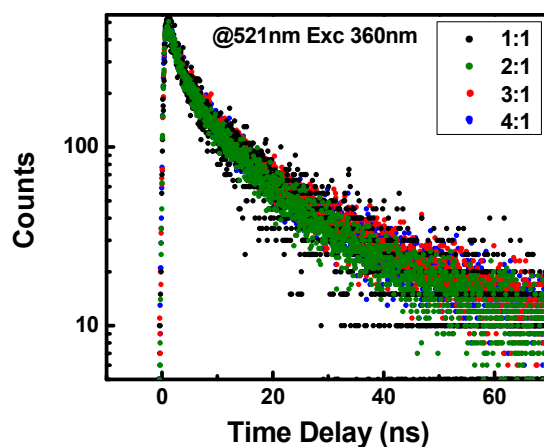


Figure 8. TCSPC measurements of 521 nm fluorescence excited at 360 nm for different molar ratios of precursors. The amplitude of the decay signal has been normalized to compare the behavior of the different samples.

Table 2. TCSPC fit parameters.

Sample	τ_1 (ns)	τ_2 (ns)
1:1	3.3 ns	17.0 ns
2:1	3.0 ns	14.7 ns
3:1	3.4 ns	16.0 ns
4:1	3.3 ns	15.1 ns

It is noteworthy that the fluorescence intensity trend clearly mirrors the variation of the (024)/(110) reflection intensity ratio in the XRD measurements (Figure 5), although the origin of such a correlation between crystalline rearrangement along a preferred plane (024) of the Cs_4PbBr_6 phase and fluorescence of CsPbBr_3 nano-inclusions is not clear.

In order to clarify the role of the two different crystalline phases, we report in Figures 9 and 10 the map of excitation for the fluorescence in the visible spectral range. On the left, the excitation spectrum of the 520 nm emission is reported for each sample. The related absorption spectra are reported for comparison. It clearly appears that, in correspondence of the UV absorption band, a strong reduction of the luminescence intensity occurs. This evidence demonstrates that Cs_4PbBr_6 phases do not directly produce visible luminescence. In order to correctly attribute the different spectral contributions, PL spectra have been generated by optical excitation with light having sufficient photon energy to excite both phases. The UV-PL spectra are shown in Figure 11 for sample 4:1. The strong UV fluorescence at 375 nm, which we attribute to the Cs_4PbBr_6 [26,39], turns on progressively as the excitation wavelength approaches the UV absorption peak at 320 nm; the ratios of the UV- to VIS-PL peak intensities resulted as being 10%, 45% and 165%, respectively, for 260 nm, 305 nm and 320 nm. The intensity of the visible PL as a function of the exciting wavelength (Figures 9 and 10) reflects, with an inverse relationship, the light absorption by Cs_4PbBr_6 that becomes more and more important as the Cs_4PbBr_6 amount in the powder increases, as suggested by the less structured absorption band for high Cs_4PbBr_6 content and the ensuing decrease of relative importance of the absorption by the CsPbBr_3 . This feature suggests a shadowing of the CsPbBr_3 inclusions by the surrounding Cs_4PbBr_6 . However, the overall picture must also include a possible charge transfer between the two phases. To this scope we have performed the time-resolved measurements on the UV luminescence (not reported) showing that the UV luminescence lifetime is shorter than the IRF of our set-up. This result suggests the presence of some trapping into the

CsPbBr_3 of photoexcited carriers in the Cs_4PbBr_6 , with a characteristic time shorter than the radiative recombination time, expected to be in the ns range.

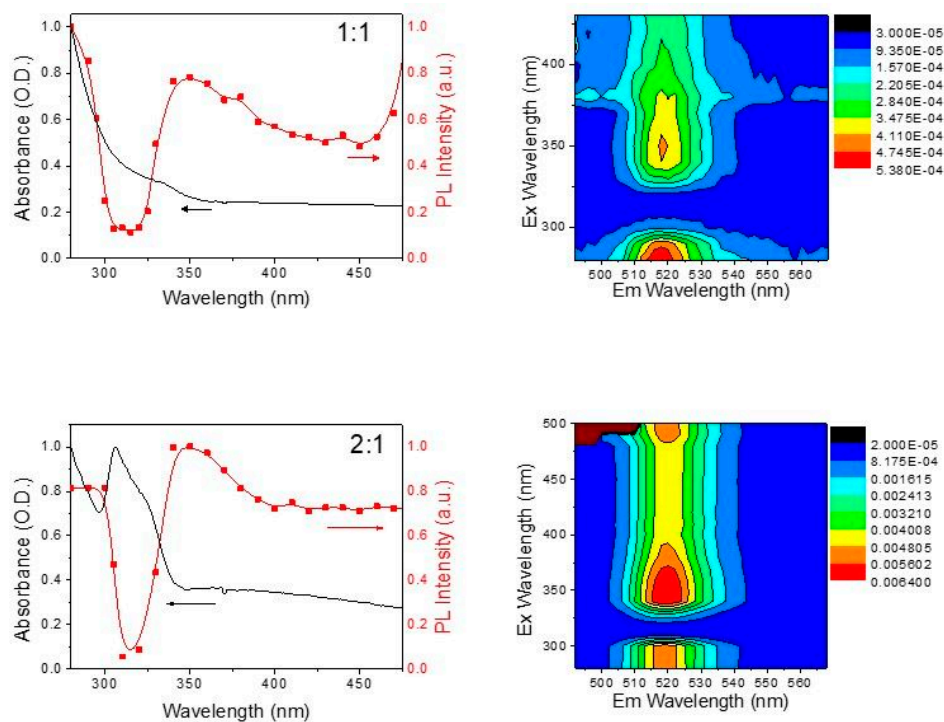


Figure 9. Excitation spectra ($\lambda_{\text{em}} = 520$ nm, red squares) and contour curves of the fluorescence for 1:1 and 2:1 samples. The respective absorption spectra (black lines) from Figure 6 are also reported for comparison.

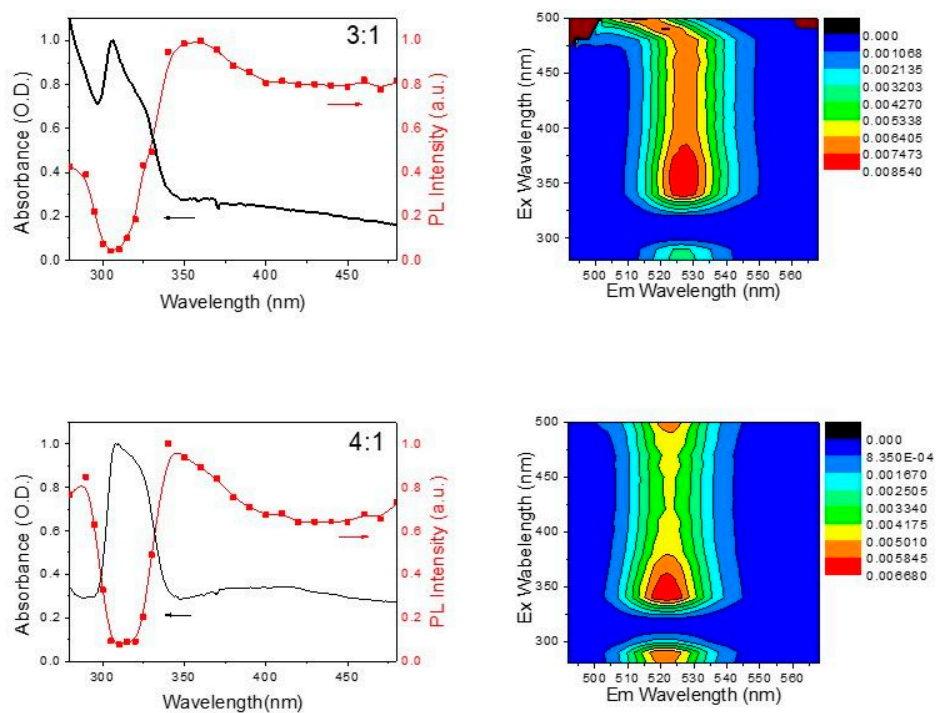


Figure 10. Excitation spectra ($\lambda_{\text{em}} = 520$ nm, red squares) and contour curves of the fluorescence for 3:1 and 4:1 samples. The respective absorption spectra (black lines) from Figure 6 are also reported for comparison.

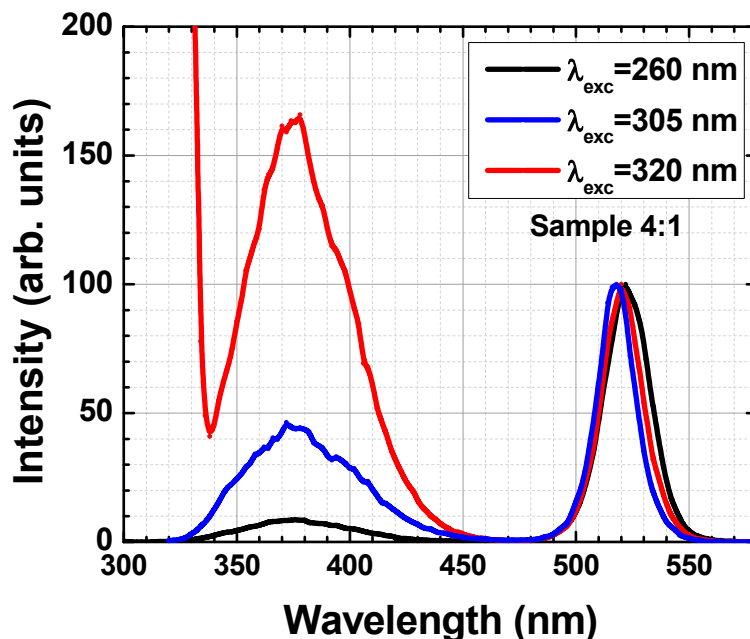


Figure 11. PL spectrum for 4:1 sample excited at different wavelengths in the UV spectral range. The intensity is normalized at the VIS-PL peak.

4. Conclusions

The structural and optical properties of an inorganic metal halide perovskite (cesium lead bromide) as a function of the composition were investigated. The samples have been characterized by X-ray diffraction measurements in order to investigate the distribution of the different crystalline phases. The XRD patterns match the presence of three phases: a monoclinic CsPbBr_3 phase associated with a spurious tetragonal CsPb_2Br_5 and rhombohedral Cs_4PbBr_6 phase. The former two structures were observed in the samples which had been deposited from equimolar Cs/Pb precursor solution while the latter in those from the precursor solutions with a cesium excess.

A preferential orientation of Cs_4PbBr_6 crystallites along the (024) crystalline plane has been observed as a function of the molar ratio of the Cs/Pb precursor salts. The degree of preferential orientation of the crystallites is mirrored in an increase in fluorescence intensity although the correlation between the two properties is not clear. The excitation spectra of the green fluorescence (520 nm) was recorded over an extended spectral range down to 280 nm. We observed a sharp reduction of the excitation efficiency in correspondence of the characteristic UV absorption band at 324 nm. The Cs_4PbBr_6 photoluminescence which peaked at 365 nm has been measured by optical excitation in correspondence of the UV absorption band. This allowed us to relate the UV absorption structure to the fundamental band–band transition of Cs_4PbBr_6 .

Overall, the present study supports the hypothesis that the Cs_4PbBr_6 perovskite phase is not fluorescent in the visible range, but it shows a strong UV luminescence, while the efficient green fluorescence comes from the CsPbBr_3 nano-inclusions inside the Cs_4PbBr_6 matrix.

Author Contributions: Supervision, F.D.M.; investigation, F.V., S.P., E.C., A.G., L.D.M., and J.S.P.C.; writing—review & editing, F.D.M., R.P., B.P., F.M. and P.P.; funding acquisition P.P.

Funding: This research was funded by Regione Lazio, through Progetto di ricerca 85-2017-15125, according to L.R.13/08.

Acknowledgments: The authors gratefully acknowledge V. Mirruzzo for diffuse absorption measurements at Choose Lab (Polo Solare Organico Regione Lazio) and Marco Guaragno (ISM-CNR) for his technical support with XRD experiments.

Conflicts of Interest: The authors declare no conflict of interest. The funders had no role in the design of the study; in the collection, analyses, or interpretation of data; in the writing of the manuscript, or in the decision to publish the results.

References

1. Editorial. Perovskites keep on giving. *Nat. Mater.* **2018**, *17*, 371. [[CrossRef](#)] [[PubMed](#)]
2. Green, M.A.; Ho-Baillie, A.; Snaith, H.J. The emergence of perovskite solar cells. *Nature Phot.* **2014**, *8*, 506–514. [[CrossRef](#)]
3. Berry, J.; Buonassisi, T.; Egger, D.A.; Hodes, G.; Kronik, L.; Loo, Y.-L.; Lubomirsky, I.; Marder, S.R.; Mastai, Y.; Miller, J.S.; et al. Hybrid Organic-Inorganic Perovskites (HOIPs): Opportunities and Challenges. *Adv. Mater.* **2015**, *27*, 5102–5112. [[CrossRef](#)]
4. Snaith, H.J. Present status and future prospects of perovskite photovoltaics. *Nature Mater.* **2018**, *17*, 372–376. [[CrossRef](#)]
5. Paci, B.; Generosi, A.; Wright, J.; Ferrero, C.; Di Carlo, A.; Brunetti, F. Planar Perovskite Solar Cells: Local Structure and Stability Issues. *Sol. RRL* **2017**, *1*, 1700066. [[CrossRef](#)]
6. Kakavelakis, G.; Paradisanos, I.; Paci, B.; Generosi, A.; Papachatzakis, M.; Maksudov, T.; Najafi, L.; Esaú Del Rio Castillo, A.; Kioseoglou, G.; Stratakis, E. Extending the Continuous Operating Lifetime of Perovskite Solar Cells with a Molybdenum Disulfide Hole Extraction Interlayer. *Adv. Energy Mater.* **2018**, *8*, 1702287. [[CrossRef](#)]
7. Baretin, D.; Di Carlo, A.; De Angelis, R.; Casalboni, M.; Proposito, P. Effect of dielectric Bragg grating nanostructuring on dye sensitized solar cells. *Opt. Expr.* **2012**, *20*, A888–A897. [[CrossRef](#)]
8. Yantara, N.; Bhaumik, S.; Yan, F.; Sabba, D.; Dewi, H.A.; Mathwes, N.; Boix, P.P.; Demir, H.V.; Mhaisalkar, S. Inorganic Halide Perovskites for Efficient Light-Emitting Diodes. *J. Phys. Chem. Lett.* **2015**, *6*, 4360–4364. [[CrossRef](#)]
9. Xu, J.; Huang, W.; Li, P.; Onken, D.R.; Dun, C.; Guo, Y.; Ucer, K.B.; Lu, C.; Wang, H.; Geyer, S.M.; et al. Imbedded Nanocrystals of CsPbBr₃ in Cs₄PbBr₆: Kinetics, Enhanced Oscillator Strength, and Application in Light-Emitting Diodes. *Adv. Mater.* **2017**, *29*, 1703703. [[CrossRef](#)]
10. Chakraborty, A.; Pizzoferrato, R.; Agresti, A.; De Matteis, F.; Orsini, A.; Medaglia, P.G. Wet-chemical synthesis of ZnO nanowires on low temperature photo-activated ZnO-rGO composite thin film with enhanced photoconduction. *J. Electr. Mater.* **2018**, *10*, 5863–5869. [[CrossRef](#)]
11. Veldhuis, S.A.; Boix, P.P.; Yantara, N.; Li, M.; Sum, T.C.; Mathews, N.; Mhaisalkar, S.G. Perovskite Materials for Light-Emitting Diodes and Lasers. *Adv. Mater.* **2016**, *28*, 6804–6834. [[CrossRef](#)]
12. Suzuki, H.; Ogura, K.; Matsumoto, N.; Schutzmann, S. Polymethine Dyes as Novel Efficient Infrared Electroluminescence Materials. *Mol. Cryst. Liq. Cryst.* **2006**, *444*, 51–59. [[CrossRef](#)]
13. Lamastra, F.R.; De Angelis, R.; Antonucci, A.; Salvatori, D.; Proposito, P.; Casalboni, M.; Congestri, R.; Melino, S.; Nanni, F. Polymer composite random lasers based on frustules as scatterers. *RSC Adv.* **2014**, *4*, 61809–61816. [[CrossRef](#)]
14. Wei, H.; Fang, Y.; Mulligan, P.; Chuirazzi, W.; Fang, H.-H.; Wang, C.; Ecker, B.R.; Gao, Y.; Loi, M.A.; Cao, L. Sensitive X-ray detectors made of methylammonium lead tribromide perovskite single crystals. *Nat. Photonics* **2016**, *10*, 333–339. [[CrossRef](#)]
15. Dohner, E.R.; Hoke, E.T.; Karunadasa, H.I. Self-Assembly of Broadband White-Light Emitters. *J. Am. Chem. Soc.* **2014**, *136*, 1718–1721. [[CrossRef](#)]
16. Yuan, Z.; Zhou, C.; Tian, Y.; Shu, Y.; Messier, J.; Wang, J.C.; van de Burgt, L.J.; Kountouriotis, K.; Xin, Y.; Holt, E.; et al. One-dimensional organic lead halide perovskites with efficient bluish white-light emission. *Nat. Commun.* **2017**, *8*, 14051. [[CrossRef](#)]
17. Zhou, C.; Lin, H.; Tian, Y.; Yuan, Z.; Clark, R.J.; Chen, B.; van de Burgt, B.; Wang, J.C.; Zhou, Y.; Hanson, K. Luminescent zero-dimensional organic metal halide hybrids with near-unity quantum efficiency. *Chem. Sci.* **2018**, *9*, 586–593. [[CrossRef](#)] [[PubMed](#)]
18. Dong, Q.; Fang, Y.; Shao, Y.; Mulligan, P.; Qiu, J.; Cao, L.; Huang, J. Electron-hole diffusion lengths > 175 μm in solution-grown CH₃NH₃PbI₃ single crystals. *Science* **2015**, *347*, 967–970. [[CrossRef](#)] [[PubMed](#)]

19. Xing, G.; Mathews, N.; Sun, S.; Lim, S.S.; Lam, Y.M.; Graetzel, M.; Mhaisalkar, S.; Sum, T.C. Long-Range Balanced Electron- and Hole-Transport Lengths in Organic-Inorganic $\text{CH}_3\text{NH}_3\text{PbI}_3$. *Science* **2013**, *342*, 344–347. [[CrossRef](#)] [[PubMed](#)]
20. Zuo, C.; Bolink, H.J.; Han, H.; Huang, J.; Cahen, D.; Ding, L. Advances in Perovskite Solar Cells. *Adv. Sci.* **2016**, *3*, 1500324. [[CrossRef](#)]
21. Han, D.; Shi, H.; Ming, W.; Zhou, C.; Ma, B.; Saparov, B.; Ma, Y.Z.; Chen, S.; Du, M.H. Unraveling luminescence mechanisms in zero-dimensional halide perovskites. *J. Mater. Chem. C* **2018**, *6*, 6398. [[CrossRef](#)]
22. Saidaminov, M.I.; Almutlaq, J.; Sarmah, S.; Dursun, I.; Zhumekenov, A.A.; Begum, R.; Pan, J.; Cho, N.; Mohammed, O.F.; Bakr, O.M. Pure Cs_4PbBr_6 : Highly Luminescent Zero-Dimensional Perovskite Solids. *ACS Energy Lett.* **2016**, *1*, 840–845. [[CrossRef](#)]
23. De Bastiani, M.; Dursun, I.; Zhang, Y.; Alshankiti, B.A.; Miao, X.H.; Yin, J.; Yengel, E.; Alarousu, E.; Turedi, B.; Almutlaq, J.M.; et al. Inside Perovskites: Quantum Luminescence from Bulk Cs_4PbBr_6 Single Crystals. *Chem. Mater.* **2017**, *29*, 7108. [[CrossRef](#)]
24. Zhang, Y.; Saidaminov, M.I.; Dursun, I.; Yang, H.; Alarousu, B.E.; Yengel, E.; Alshankiti, B.A.; Bakr, O.M.; Mohammed, O.F. Zero-dimensional Cs_4PbBr_6 Perovskite Nanocrystals. *J. Phys. Chem. Lett.* **2017**, *8*, 961–965. [[CrossRef](#)]
25. Cha, J.-H.; Han, J.; Yin, W.; Park, C.; Park, Y.; Ahn, T.K.; Cho, J.H.; Jung, D.-Y. Photoresponse of CsPbBr_3 and Cs_4PbBr_6 Perovskite Single Crystals. *J. Phys. Chem. Lett.* **2017**, *8*, 565–570. [[CrossRef](#)]
26. Nikl, M.; Mihokova, E.; Nitsch, K.; Somma, F.; Giampaolo, C.; Pazzi, G.P.; Fabeni, P.; Zazubovich, S. Photoluminescence of Cs PbBr crystals and thin films. *Chem. Phys. Lett.* **1999**, *306*, 280–284. [[CrossRef](#)]
27. Riesen, N.; Lockrey, M.N.; Badek, K.; Riesen, H. On the origins of the green luminescence in the “zero-dimensional perovskite” Cs_4PbBr_6 : Conclusive results from cathodoluminescence imaging. *Nanoscale* **2019**, *11*, 3925–3932. [[CrossRef](#)] [[PubMed](#)]
28. Chen, X.; Zhang, F.; Ge, Y.; Shi, L.; Huang, S.; Tang, J.; Lv, Z.; Zhang, L.; Zou, B.; Zhong, H. Centimeter-Sized Cs_4PbBr_6 Crystals with Embedded CsPbBr_3 Nanocrystals Showing Superior Photoluminescence: Nonstoichiometry Induced Transformation and Light-Emitting Applications. *Adv. Funct. Mater.* **2018**, *28*, 1706567. [[CrossRef](#)]
29. Burratti, L.; De Matteis, F.; Casalboni, M.; Francini, R.; Pizzoferrato, R.; Proposito, P. Polystyrene photonic crystals as optical sensors for volatile organic compounds. *Mat. Chem. Phys.* **2018**, *212*, 274–281. [[CrossRef](#)]
30. Ciotta, E.; Paoloni, S.; Richetta, M.; Proposito, P.; Tagliatesta, P.; Lorecchio, C.; Venditti, I.; Fratoddi, I.; Casciardi, S.; Pizzoferrato, R. Sensitivity to Heavy-Metal Ions of Unfolded Fullerene Quantum Dots. *Sensors* **2017**, *17*, 2614. [[CrossRef](#)]
31. Ricci, A.; Chiarini, M.; Sterzo, C.L.; Pizzoferrato, R.; Paoloni, S. Synthesis and photophysical properties of poly (arylene ethynylene) small-molecules and polymers derivatized with leucine substituents. *J. Photochem. Photobiol. A Chem.* **2015**, *298*, 1–8. [[CrossRef](#)]
32. Moller, C.K. The structure of perovskite-like caesium plumbo CsPbI_3 . *Mat.-Fys. Medd. K. Dan. Vidensk. Selsk.* **1959**, *32*, 1.
33. Moller, C.K. Electrochemical investigation of the transition from tetragonal to cubic caesium plumbo chloride. *Mat.-Fys. Medd. K. Dan. Vidensk. Selsk.* **1960**, *32*, 3.
34. Cola, M.; Massarotti, V.; Riccardi, R.; Sinistri, C.Z. Binary Systems Formed by Lead Bromide with (Li, Na, K, Rb, Cs and Tl)Br: a DTA and Diffractometric Study. *Naturforsch. A* **1971**, *26*, 1328. [[CrossRef](#)]
35. Rakita, Y.; Kedem, N.; Gupta, S.; Sadhanala, A.; Kalchenko, V.; Bohm, M.L.; Kulbak, M.; Friend, R.H.; Cahen, D.; Hodes, G. Low-Temperature Solution-Grown CsPbBr_3 Single Crystals and Their Characterization. *Cryst. Growth Des.* **2016**, *16*, 5717–5725. [[CrossRef](#)]
36. Shi, Z.; Li, Y.; Zhang, Y.; Chen, Y.; Li, X.; Wu, D.; Xu, T.; Shan, C.; Du, G. High-efficiency and air-stable perovskite quantum dots light-emitting diodes with all-inorganic heterostructure. *Nano Lett.* **2017**, *17*, 313–321. [[CrossRef](#)]
37. Yang, L.; Li, D.; Wang, C.; Yao, W.; Wang, H.; Huang, K. Room-temperature synthesis of pure perovskite-related Cs_4PbX_6 nanocrystals and their ligand-mediated evolution into highly luminescent CsPbBr_3 nanosheets. *J. Nanopart. Res.* **2017**, *19*, 258. [[CrossRef](#)]

38. Akkerman, Q.A.; Radicchi, E.; Park, S.; Nunzi, F.; Mosconi, E.; De Angelis, F.; Brescia, R.; Rastogi, P.; Prato, M.; Manna, L. Nearly Monodisperse Insulator Cs_4PbX_6 ($X = \text{Cl}, \text{Br}, \text{I}$) Nanocrystals, Their Mixed Halide Compositions, and Their Transformation into CsPbX_3 Nanocrystals. *Nano Lett.* **2017**, *17*, 1924–1930. [[CrossRef](#)] [[PubMed](#)]
39. Babin, V.; Fabeni, P.; Mihokova, E.; Nikl, M.; Pazzi, G.P.; Zazubovich, N.; Zazubovich, S. Luminescence of Cs_4PbBr_6 aggregates in As-grown and in annealed $\text{CsBr}:\text{Pb}$ single crystals. *Phys. Status Solidi B* **2000**, *219*, 205–214. [[CrossRef](#)]
40. Chen, Y.-M.; Zhou, Y.; Zhao, Q.; Zhang, J.-Y.; Ma, J.-P.; Xuan, T.-T.; Guo, S.-Q.; Yong, Z.-J.; Wang, J.; Kuroiwa, Y.; et al. $\text{Cs}_4\text{PbBr}_6/\text{CsPbBr}_3$ Perovskite Composites with Near-Unity Luminescence Quantum Yield: Large-Scale Synthesis, Luminescence and Formation Mechanism, and White Light-Emitting Diode Application. *ACS Appl. Mater. Interfaces* **2018**, *10*, 15905–15912. [[CrossRef](#)] [[PubMed](#)]
41. Quan, L.N.; Quintero-Bermudez, R.; Voznyy, O.; Walters, G.; Jain, A.; Fan, J.Z.; Zheng, X.; Yang, Z.; Sargent, E.H. Highly Emissive Green Perovskite Nanocrystals in a Solid State Crystalline Matrix. *Adv. Mater.* **2017**, *29*, 1605945. [[CrossRef](#)]
42. De Angelis, R.; Casalboni, M.; De Matteis, F.; Hatami, F.; Masselink, W.T.; Zhang, H.; Proposito, P. Chemical sensitivity of $\text{InP}/\text{In}_{0.48}\text{Ga}_{0.52}\text{P}$ surface quantum dots studied by time-resolved photoluminescence spectroscopy. *J. Lumin.* **2015**, *168*, 54–58. [[CrossRef](#)]
43. Tian, Y.; Scheblykin, I.G. Artifacts in Absorption Measurements of Organometal Halide Perovskite Materials: What Are the Real Spectra? *J. Phys. Chem. Lett.* **2015**, *6*, 3466–3470. [[CrossRef](#)]
44. Seth, S.; Samanta, A. Photoluminescence of Zero-Dimensional Perovskites and Perovskite-Related Materials. *J. Phys. Chem. Lett.* **2018**, *9*, 176–183. [[CrossRef](#)]



© 2019 by the authors. Licensee MDPI, Basel, Switzerland. This article is an open access article distributed under the terms and conditions of the Creative Commons Attribution (CC BY) license (<http://creativecommons.org/licenses/by/4.0/>).